AIChE WILEY InterScience DISCOVER SOMETHING GREAT

FLUID MECHANICS AND TRANSPORT PHENOMENA

# Mixing of Shear-Thinning Fluids with Yield Stress in Stirred Tanks

**P. E. Arratia, J. Kukura, J. Lacombe, and F. J. Muzzio**
Dept. of Chemical and Biochemical Engineering, Rutgers University, Piscataway, NJ 08855

*DOI 10.1002/aic.10847*
*Published online March 31, 2006 in Wiley InterScience (www.interscience.wiley.com).*

*Mixing of shear-thinning fluids with yield stress is investigated in a three-dimensional (3-D) flow both in experiments and in simulations. Experiments are conducted in a stirred tank using tracer visualization and velocity measurements. Bulk flow visualization shows the familiar cavern formation around the impeller with stagnant zones surrounding it. Detailed flow visualization inside caverns reveals the main ingredients of chaotic flow: lobe formation, stretching, folding, and self-similar mixing patterns. For multiple impeller systems, however, we find strong compartmentalization characterized by robust segregation between adjacent caverns, hindering mixing performance. Mixing efficiency is enhanced by moving the shaft off-center, which breaks spatial symmetry. The displacement of the shaft from the tank centerline has a beneficial effect on manifold structure: segregated regions are destroyed, separatrices are eliminated, and axial circulation is improved. Numerical simulations are performed by solving the incompressible Reynolds Averaged Navier Stokes equation with a Galerkin Least-Squares finite-element formulation and a macroscopic rheological model. Simulations are able to capture the main features of the flow and are used to investigate stretching statistics and scale behavior.* © 2006 American Institute of Chemical Engineers *AIChE J,* 52: 2310–2322, 2006
*Keywords: fluid mixing, chaos, stirred tanks, yield stress, shear-thinning, complex fluids*

## Introduction

Fluid mixing is an important process in industries, nature, and everyday life. Today it is well known that simple, non-turbulent velocity fields can create complex distributions of an advected field by exponential stretching and folding of material lines and surfaces. This phenomenon is termed "chaotic advection,"[1] and it has been studied by many researchers.[2-7] A majority of previous research has been restricted to Newtonian fluids, often in model flows under idealized conditions. Most flows of industrial interest, by contrast, are three-dimensional (3-D) and complex. Further, real high viscosity fluids often contain polymers or solids (such as fermentation broths, pastes, and colloids), and they are hardly ever Newtonian. Non-Newtonian fluids are common in industry and even in the human body (such as blood, saliva, and synovial fluid). They play a significant role in the materials, biochemical, polymer, and pharmaceutical industries. Although there has been recent progress, much remains to be learned about the fundamental phenomena controlling flow and mixing of non-Newtonian fluids in 3-D flows. The basic flow phenomena are at best partially understood, and as a result design and scale-up of non-Newtonian flows in mixing and reaction operations is difficult.

Shear-thinning viscosity and yield stress (viscoplastic) behavior are very common properties of non-Newtonian fluids. Such materials are frequently encountered in industrial problems (such as pastes and suspensions). Although the concept of yield stress is often challenged (see Ref. 8 for a review), its physical approximation has proved very useful in a wide range of applications, including mixing. For example, Wichterle and Wein[9] showed that, in a stirred tank, a yield stress fluid is mobile around the impeller where shear stresses are high, whereas the same fluid is stagnant away from the impeller

Correspondence concerning this article should be addressed to F. J. Muzzio at muzzio@soemail.rutgers.edu.

where shear stresses are low. Mobile regions are often called "caverns." Several studies attempted to correlate cavern size to the amount of energy introduced to the system via torque measurements using empirical models.[10-14] Such models improved over the years by assuming different cavern shapes (spherical, cylindrical, and toroidal), accounting for different forces (tangential and axial[15]), assuming different flow regimes inside the cavern,[16] and using different rheological models. Although these models are able to predict the cavern size under a range of operating conditions, they are highly specific to the geometry and fluid considered. They provide limited insight into the general mixing mechanism of shear-thinning yield stress fluids.

Most flows of industrial relevance are 3-D. Numerical simulation of such flows is far from trivial due, in part, to complex geometry. Recent advances on numerical algorithms and discretization methods have allowed the study of chaotic mixing in 3-D flows with reasonable success.[17-21] One advantage of numerical simulations is that, once a validated solution is obtained, they can provide a wealth of information that would be difficult to obtain experimentally. For shear-thinning yield stress fluids, numerical simulations must also be combined with a proper rheological model. Although mixing of yield stress fluids in industrially relevant devices is of interest, the majority of the previous numerical studies have been restricted to 2-D flows.[22-25] In such flows stagnant regions and plugs with rigid rotation have been encountered, which indicates that mixing of yield stress fluids is far from trivial. The investigation of mixing of yield stress fluids in 2-D flows has been thorough. It has laid the foundation for the advances in numerical methods and rheological models that can be used to investigate 3-D flows. Numerical investigations into the mixing of yield stress fluids in 3-D systems[13,26-29] have been conducted with different levels of success. In some cases good agreement between experimental and simulated velocity fields is achieved. However, as with previous experimental investigations, most studies focused on empirical relationships that are highly specific. The Lagrangian properties of the flow are seldom analyzed.

In this article, we investigate the effects of shear-thinning viscosity and yield stress (viscoplastic) behavior on mixing in a 3-D flow using experiments and numerical simulations. A 3-D flow is generated in a stirred tank equipped with Rushton impellers. Mixing is investigated in experiments by means of velocity measurements and tracer visualizations. Symmetry-breaking methods are used to investigate mixing "performance." Numerical simulations of shear-thinning viscoplastic fluids are performed using CFD and a viscosity model, which is based on rheological measurements. Stretching statistics and scale behavior are investigated using simulations.

## Experimental Methods

### *Rheology*

Two fluids are in consideration in this article: Glycerin (USP grade, 99.7%; Brown Chemicals, NJ) and Carbopol 940 (BF Goodrich). Glycerin is used to investigate Newtonian fluid behavior. Shear-thinning viscosity and yield stress behavior is investigated using an aqueous Carbopol solution (0.1% by weight).

The Carbopol solution is characterized using a stress-controlled cone-plate rheometer (SR-2000, Rheometric Scientific, Piscataway, NJ). The cone-plate is 40 mm in diameter and the cone angle is 0.0394 radians. The gap between the cone and the stationary plate is maintained constant at 0.0787 mm. The viscosity versus shear rate ($\dot{\gamma}$) data show a drop in viscosity (Figure 1) of up to 5 decades with a power-law index ($n$) of 0.7. The zero-shear-rate-viscosity ($\eta_0$) and the infinite-shear-rate viscosity ($\eta_\infty$) are approximated to 1100 Pa·s and 0.75 Pa·s, respectively. The stress-strain curve shows that the fluid also has a marked yield stress component (Figure 1, secondary y-axis) of approximately 1.6 Pa. The first normal stress difference, characteristic of viscoelastic fluids, is low (on the order of $10^{-3}$ Pa). Hence, viscoelastic effects are neglected.

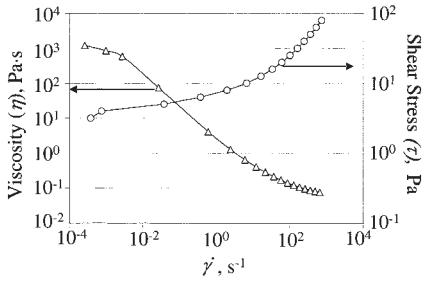


**Figure 1. Fluid viscosity (primary y-axis) and stress (secondary y-axis) as a function of shear rate for a 0.1% (w/w) aqueous solution of Carbopol.**

### *Systems and flow geometry*

All experiments are performed in a custom-made Plexiglas™ vessel equipped with an illumination and image-acquisition system (Figure 2a). We investigate the flow of two different system configurations: a single Rushton impeller and a three-equidistant Rushton impellers, shown in Figures 2b and 2c, respectively. The Rushton impellers are 7.5 cm in diameter and placed concentrically in the tank along a single shaft. In the case of the 3-impeller system, the distance between impellers is 9 cm, measured from impeller mid-plane. The distance between the lower impeller and the tank bottom is 9 cm for both systems. The distance between the highest impeller and the tank free surface is 9 cm for the 3-impeller system.

The vessel geometry consists of a flat-bottom cylinder surrounded by a square Plexiglas™ outer box to eliminate optical aberration due to cylindrical walls. The tank height is 40 cm and its diameter is 24 cm. The tank fill levels are 32 cm and 36 cm for the single and the 3-agitator system, respectively. The agitators are driven by a controlled DC-motor. For all experiments, the tank is allowed to sit overnight to eliminate air bubbles that might have been entrained during pumping or filling.

In this article, the Reynolds number, $Re = \rho\Omega D_I^2/\mu$, for the Newtonian fluid (Glycerin) is based on the impeller diameter $D_I = 7.5$ cm, impeller speed $\Omega$ (in Hz), fluid density $\rho$ (1.2 kg/m$^3$), and viscosity $\mu$ (0.7 Pa·s). For the shear-thinning fluid, we define $Re' = \rho\Omega D_I^2/\eta$, where $\eta$ is the shear rate-dependent fluid viscosity. Values of $\eta$ are taken from rheological measurements at the same shear-rate ($\dot{\gamma}$) as the impeller speed ($\Omega$).

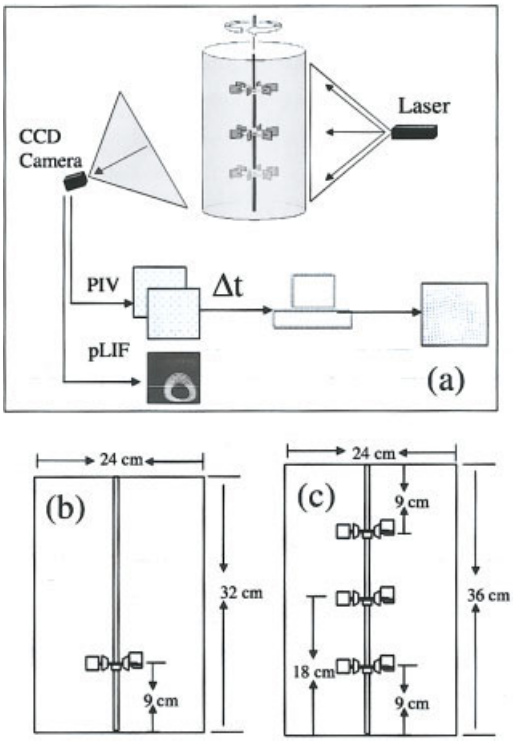


**Figure 2. (a) PIV and pLIF experimental set-up; (b) Single Rushton and (c) 3-Rushton impeller configuration tank schematics and dimensions (drawing not to scale).**

[Color figure can be viewed in the online issue, which is available at www.interscience.wiley.com.]

### *Flow visualization*

Two tracer visualization techniques are employed in this study: planar laser induced fluorescence (pLIF) and ultraviolet (UV) fluorescence. The main advantage of both visualization techniques is that they are non-intrusive. A description of the mixing process is assessed by the location of a neutrally buoyant dye as a function of time.

In pLIF, a laser beam, generated by a light source, transversally cuts the cylinder plane. This technique is used for two-dimensional (2-D) imaging by forming the laser beam into a sheet and then passing it through the flow. By using a camera placed at right angles to the laser sheet, an image is obtained revealing the detailed distribution of the tracer in the flow.

Rhodamine B is used as the passive tracer for pLIF experiments since it has strong absorption bands at 532 nm with peaks of fluorescent emission at 560 nm. To discriminate against scattered laser light and to remove natural luminosity from the flow, a 552-nm filter is used. Experiments are performed using a 32-mJ NewWave Nd:YAG pulsing laser, which provides a homogeneous thin laser sheet at 532 nm with frequencies up to 50 Hz. The laser sheet is positioned vertically across the cylinder plane about 1 cm behind the shaft such that light would not be blocked. Experiments are recorded using a Nikon 35-mm and CCD cameras. Further details on pLIF may be found elsewhere.[30]

UV fluorescence is one of the simplest visualization techniques for fluid mixing, requiring only a suitable fluorescent dye. We use fluorescein as the passive tracer for UV experiments. Fluorescein is usually excited at 458 nm and emits at 530 nm. Light is emitted continuously using two UV lamps that are placed directly on top of the tank, sampling the entire vessel and providing valuable information on bulk flow behavior and 3-D flow structures.

Both dye solutions are prepared by dissolving the powdered dye into the model-fluid of interest until neutral buoyancy is achieved. Dye injections are prepared using small quantities of dye, $1 \times 10^{-3}$ mol/liter, in order to avoid saturation and overexposed images. The tank is then injected with approximately 3 ml of dye solution.

### *Velocimetry*

Particle Image Velocimetry (PIV) is used to acquire 2-D velocity fields at a given plane of the vessel. The PIV experimental set-up is similar to pLIF, except that particles instead of dye are injected in the fluid. In PIV, a laser sheet cuts the stirred tank transversally. The tank is seeded with neutrally buoyant 10-micron silver-coated particles. These particles are assumed to follow the same trajectories as fluid elements. A CCD camera is used to capture images of the illuminated plane. Two successive snapshots of the illuminated plane are required in order to calculate the velocity field using the fast-Fourier transforms (FFT) cross-correlation algorithm. Here, we use a Dantec® PIV system to calculate the velocity fields, which includes the Flow Manager 3.0® software package to perform cross-correlations, averaging subroutines, noise filtering, and validation procedures.

## Computational Methods

Flow of a shear-thinning fluid with yield stress is simulated in a stirred tank agitated by Rushton impellers. The analysis of flow and mixing is based on Eulerian (such as velocity and pressure fields) and Lagrangian (such as Poincaré sections and tracer patterns) techniques. Experimental validation of simulated velocity fields and mixing patterns is carried out using UV fluorescence, pLIF, and PIV measurements.

Computational mixing analysis first requires definition of the physical boundaries of the flow domain using computer-aided-design software (ICEM CFD, Berkeley, CA). The flow domain is discretized with an unstructured tetrahedral mesh consisting of 2.05 million volumetric elements. Next, the velocity and pressure are computed for the nodes comprising each volumetric element by solving the incompressible ($\nabla \cdot \vec{u} = 0$, where $\vec{u}$ is velocity) Reynolds Averaged Navier Stokes equations with a Galerkin Least-Squares finite element formulation (AcuSolve, Acusim Software, Mountain View, CA). This iterative method provides second order accuracy with respect to spatial discretization. All of the solutions are calculated in a reference frame rotating with the impeller, and the residual convergence of the steady-state solutions is at least $10^{-4}$. Finally, post-processing analysis is performed to determine mixing patterns and mechanisms using in-house software. More details on the computational methods may be found elsewhere.[21]

In order to simulate the flow of any fluid we must relate the shear stress tensor ($\bar{\bar{\tau}}$) to the rate of deformation tensor $\bar{\bar{\Delta}} = \nabla\vec{u} + (\nabla\vec{u})^T$. For Newtonian fluids the relationship is defined simply as $\bar{\bar{\tau}} = \mu\bar{\bar{\Delta}}$, where $\mu$ is the fluid viscosity. For non-

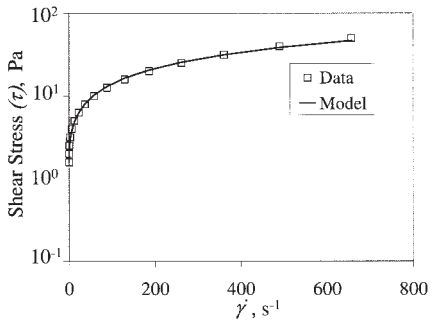


**Figure 3. Best fit of the modified Papanastasious model (Eq. 2, see text) to stress versus shear rate data for a 0.1% (w/w) aqueous solution of Carbopol.**

Newtonian fluids the relationship between shear stress and viscosity may be significantly more complex.

Fluids with yield stress (viscoplastic fluids) are commonly investigated using the Papanastasiou model[31]:

$$\bar{\bar{\tau}} = \left\{ \eta + \frac{\tau_0[1 - \exp(-M\dot{\gamma})]}{\dot{\gamma}} \right\} \bar{\bar{\Delta}}. \qquad (1)$$

Here, $M$ is the stress growth parameter, $t_0$ is the yield stress, $\dot{\gamma}$ is shear-rate, and $\eta$ is fluid viscosity. The exponent $M$ has dimensions of time (seconds) and controls the exponential raise of the stress at low strain rates. This raise is consistent with the behavior of the material in its unyielded state. In the limiting case of $\eta \rightarrow \infty$, this model reduces to the Bingham model in the yielded region.

The accuracy and effectiveness of the Papanastasiou model have been demonstrated by many researchers.[24,32,33] In this work, the Papanastasiou model is modified to account for the power-law behavior of the Carbopol solution as follows:

$$\bar{\bar{\tau}} = \left\{ \eta(\dot{\gamma})^{(n-1)} + \frac{\tau_0[1 - \exp(-M\dot{\gamma})]}{\dot{\gamma}} \right\} \bar{\bar{\Delta}}. \qquad (2)$$

This modified model has four independent material parameters whose values can be determined by fitting the model to the fluid rheological data (Figure 3). The material parameter values obtained from the best fit of the model to the data are: $\eta = 0.67$ Pa·s, $\tau_0 = 2.1$ Pa, $n = 0.7$, and $M = 500$ s. The model and the material parameter values are incorporated into the solver through a custom user-defined function.

## Review of Newtonian Laminar Mixing in Stirred Tanks

For the sake of completeness, the mechanisms of Newtonian laminar mixing in stirred tanks are briefly reviewed here (see Ref. 34 for a more in depth discussion). It has been well established that chaos is necessary in order to achieve efficient laminar mixing in stirred tanks.[18,34-36] Chaotic mixing is characterized by the exponential rate of stretching and folding of fluid elements. The repeated application of this stretching and folding engine increases the inter-material area exponentially and consequently reduces the scale of segregation of the system also at an exponential rate. Thus, it is desirable to extend the chaotic region for as much of the system as possible.

To illustrate the importance of chaos on laminar mixing, let us consider a tank stirred by a single axisymmetric *disk*. In Figure 4a, a pLIF snapshot through the axis of the mixing tank filled with a Newtonian fluid at $Re = 30$ reveals closely spaced, concentric sets of rings around elliptic points. The snapshot demonstrates that fluid does not mix down to a very small length-scale. As expected, no signs of chaotic mixing are observed since at low $Re$ the flow is an effectively steady 2-D integrable system (every azimuthal slice through the system is identical). This situation is characterized by a linear rate of stretching, and mixing is very inefficient.

We can induce chaos in the system by replacing the disk by impellers, such as the Rushton turbine. In this case ($Re = 40$), six-evenly-spaced blades perturb the base flow periodically during each passage, triggering the stretching and folding of material (a fingerprint of chaos) responsible for efficient mixing (Figure 4b). The pLIF snapshot reveals the presence of lobe structures that are periodically ejected from the impellers towards the wall. The presence of blades also adds geometric complexity to the flow since the system loses its azimuthal symmetry, becoming a three-dimensional (3-D) flow. However, robust segregated regions, illustrated by the dark region surrounded by dye, are present despite the perturbation imposed by the blades. These regions, also known as KAM (Kolmogorov-Arnold-Moser) torii or isolated mixing regions,[37] coexist with chaotic regions. No material is exchanged between segregated regions and the chaotic domain other than by diffusion. This slow exchange of material imposes obvious obstacles for efficient mixing and causes several adverse effects. Next, we explore how this picture changes when we replace the Newtonian fluid by a shear-thinning yield stress fluid.

## Mixing of Shear-Thinning Yield Stress Fluids

In this section, we begin our discussion of mixing of shear-thinning yield stress (viscoplastic) fluids. UV visualization

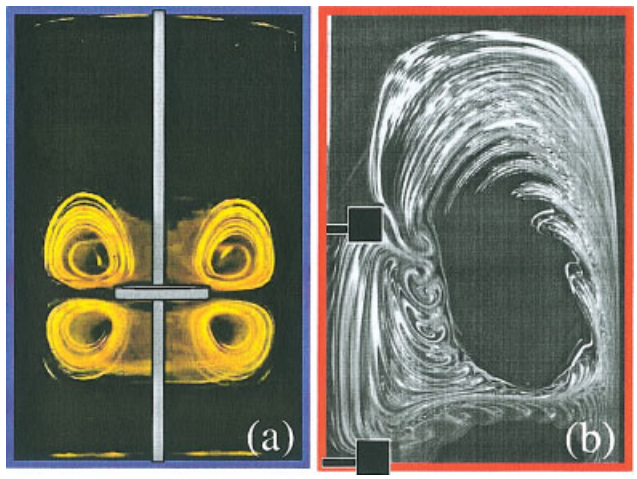


**Figure 4. (a) Flow patterns of a tank stirred by an axisymmetric disk.**

Newtonian mixing at $Re = 30$ reveals concentric rings and no signs of chaos. (b) Lobe formation and chaotic motion of a Newtonian fluid in a tank stirred by Rushton impellers at $Re = 40$. [Color figure can be viewed in the online issue, which is available at www.interscience.wiley.com.]

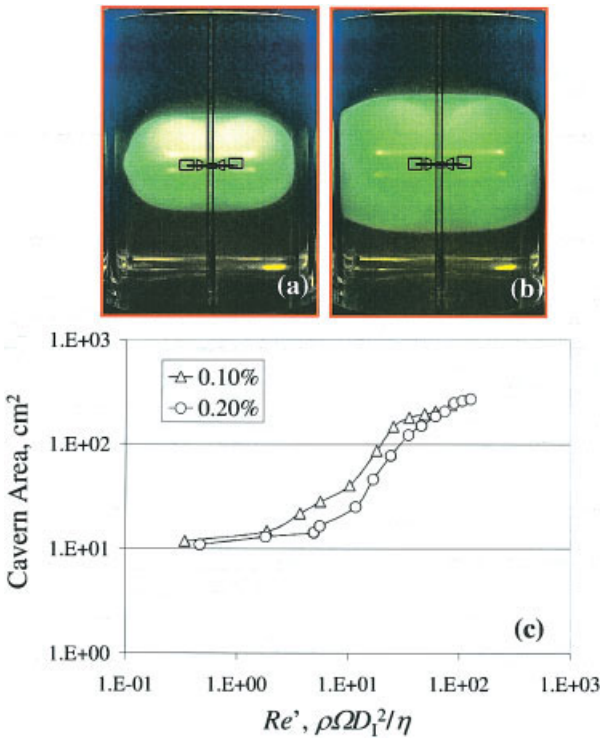


**Figure 5. Mixing of shear-thinning yield stress fluids.**

Cavern formation in a tank stirred by a single Rushton impeller at (a) $Re' = 35.1$ (300 RPM) and (b) $Re' = 90.2$ (500 RPM). Caverns are visualized using UV fluorescence. (c) Experimentally measured cavern size (area) as function of $Re'$ for two shear-thinning yield stress fluids with different Carbopol concentration. [Color figure can be viewed in the online issue, which is available at www.interscience.wiley.com.]

experiments confirm previously reported bulk flow behavior, such as the presence of caverns,[12,38] as shown in Figures 5a and 5b. Since any appreciable mixing happens only inside caverns, it is of interest to measure cavern size. We measure cavern size as a function of $Re'$ (Reynolds number for shear-thinning fluids defined earlier) using image analysis methods.[39] Cavern growth around the impeller is characterized by three regions, as shown in Figure 5c: (i) a plateau at small $Re'$ due to the fluid yield stress and fluid Newtonian-like viscosity at low shear rates; (ii) a rapid growth, in the absence of hard boundaries (walls), once the yield stress is overcome, which corresponds to the power-law region of the fluid viscosity curve; and (iii) a second plateau at higher $Re'$ corresponding to the fluid infinite-shear-viscosity. This trend is also observed in a more concentrated (0.2%) Carbopol solution.

We observe toroidal regions inside the caverns at $Re' = 35.1$ and $Re' = 90.2$, as shown by Figures 5a and 5b, respectively. The presence of such toroidal regions is an indication that coherent ordered structures and concentration spatial heterogeneity may exist within the caverns.

Next, we consider the multiple-impeller system. Figure 6 shows cavern formation at $Re' = 1.7$, $Re' = 11.7$, $Re' = 35.1$, and $Re' = 90.2$. Dyes of different colors and concentrations are injected at the blade tip of each impeller in order to distinguish the caverns. Remarkably, as agitation speed is increased, we note that caverns do not mix with each other; there is strong segregation between them. As a result, the system is effectively divided into *as many separate mixing zones as the number of impellers used*. There seems to be very little mixing between the caverns or compartments (other than diffusion) even at high agitation speeds $Re' = 90.2$ (500 RPM).

Velocimetry measurements are used to investigate in detail the velocity fields inside caverns. Since at low $Re'$ the flow is time-periodic (impeller blades disturb the fluid during each passage), we can average many instantaneous velocity fields taken at the same phase of the period. This phase-averaging increases our spatial resolution and reduces measurement noise near boundaries (such as impellers, walls, and free surfaces) and in regions of very low velocities. Phase-averaging is only used for low $Re'$ cases ($1 < Re' < 15$). For $Re' > 15$, we use the instantaneous velocity field data. An example of an instantaneous velocity field at $Re' = 61.4$ is shown in Figure 7a. We focus the measurements in a region situated between the upper and the lower impeller. In general, the velocity field within the yielded region is very similar to Newtonian laminar cases.[21] Velocity measurements show fluid being ejected from the impeller radially toward the tank walls, or in this case, the

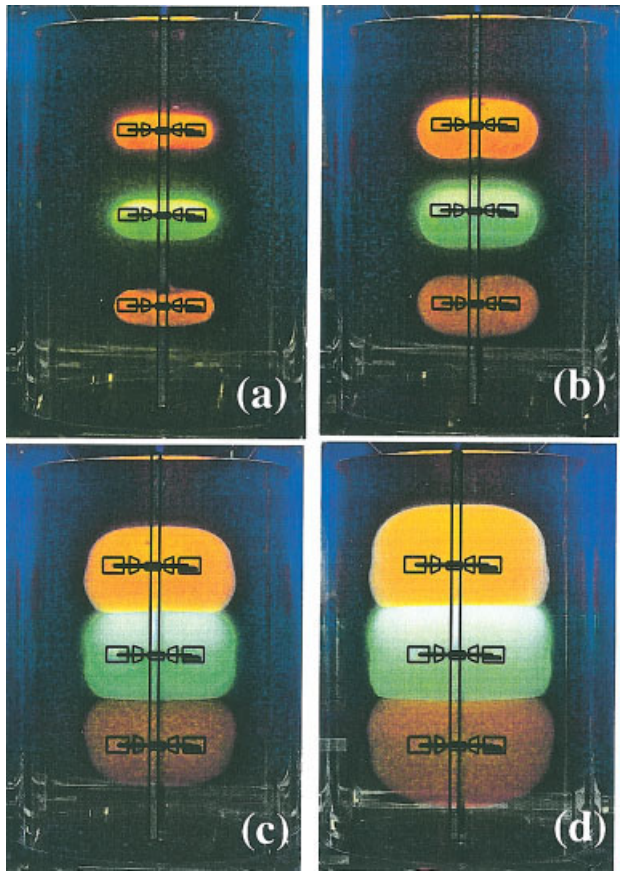


**Figure 6. UV visualization experiments in a 3-Rushton impeller system using fluorescein (green) and two concentrations of rhodamine (red) at (a) $Re' = 1.7$ (50 RPM), (b) $Re' = 11.7$ (150 RPM), (c) $Re' = 35.1$ (300 RPM), and (d) $Re' = 90.2$ (500 RPM).**

Tracer visualization reveals robust segregation between caverns even at high agitation speeds (d). [Color figure can be viewed in the online issue, which is available at www.interscience.wiley.com.]

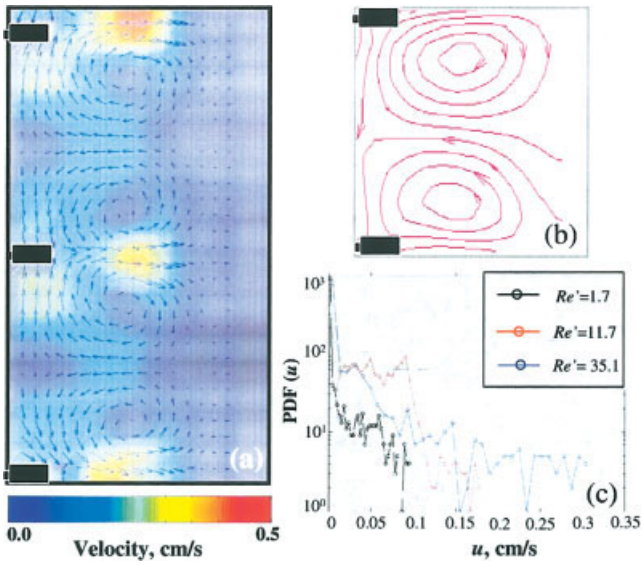


**Figure 7. (a) Instantaneous velocity field of a shear-thinning yield stress fluid obtained using PIV in a region between the lower and upper impeller at $Re' = 61.4$.**

(b) Corresponding streamlines in a region between the upper and middle impeller. (c) Probability density function (PDF) of the magnitude of the velocities at various $Re'$. [Color figure can be viewed in the online issue, which is available at www.interscience.wiley.com.]

cavern "wall," where it reaches the limit of the yield stress region. Fluid then moves axially and curves towards the tank center line where it is re-injected toward the impellers. We also find strong tangential lines that do not cross or intersect each other. They are situated midway between impellers and they are probably related to the strong boundary between caverns that leads to segregation.

Another way to visualize the velocity field is to compute the flow streamlines (Figure 7b). Although streamlines are computed for the entire tank, we only show a region between the impellers. The corresponding streamlines show material being ejected radially toward the walls and being re-circulated back through the shaft. We also find secondary circulation loops within the flow above and below the impeller. These circulation regions are often associated with the presence of toroidal regions (segregated regions) in the flow.

The flow characteristics can be further analyzed by computing the probability density function (PDF) of the magnitude of the velocity ($u$) as shown in Figure 7c. The PDF of $u$ is defined as $\mathrm{PDF}(u) = \mathrm{d}p(u)/\mathrm{d}(u)$, where $\mathrm{d}p(u)$ is the number of points with values of $u$ between $u$ and $u + \mathrm{d}(u)$. The physical meaning of PDF($u$) is the relative distribution of the magnitude of the velocities from the smallest to the largest values of the selected location. We find that the velocity fields are highly heterogeneous with velocities spanning many orders of magnitude. As the shear-rate or $Re'$ is increased, the distributions get broader, which reveals the growth of the yielded regions or caverns.

We examine the mixing mechanism by tracking the evolution of flow microstructures. This is accomplished via pLIF experiments. Figure 8a shows an early pLIF snapshot of dye being convected by a Rushton impeller taken after 1 min of agitation at $Re' = 35.1$. The dye spreads into streaks that rapidly align along the unstable manifold of the flow, gradually invading the chaotic region of the cavern. The snapshot reveals the formation of lobe structures that are ejected periodically from the impeller toward the tank wall (the frequency of the pulse is 6 times that of the impeller). Lobes are then stretched, folded, and transported back to the impeller through the shaft in an elliptic trajectory surrounding the toroidal regions. Figure 8b shows that this iterative engine (stretching, folding, and transport) progressively adds features to an underlying structure that governs this mixing process; the structure is essentially the same as it was at earlier times (Figure 8a), except that a larger number of thinner striations are found in the region, which are eroded by the effects of diffusion. The formation of lobe structures and the iterative stretching and folding process are hallmarks of chaos in laminar stirred tanks, and they have also been observed in shear-thinning *viscoelastic* fluids.[40]

### *Computational results*

Numerical simulations are used to investigate flow and mixing of shear-thinning yield stress fluids in stirred tanks using Eulerian and Lagrangian approaches. As amply demonstrated by unpleasant experience, CFD results should be validated by experimental data. A CFD solution can converge well and the resulting flow field can appear reasonable at first. However, significant flow features may be absent due to insufficient mesh resolution, and seemingly minor discrepancies can profoundly affect predicted mixing behavior.[41] Validation of the work presented here is two-pronged. First, computed bulk flow patterns in a vertical plane cutting through the tank are compared with results obtained via PIV using planar projection of the velocity. Second, mixing patterns are validated by comparing flow patterns generated by computational particle tracking and dye experiments.

Figure 9a shows the instantaneous planar velocity field calculated using CFD (lefthand side) and measured using PIV (right-hand side) at $Re' = 35.1$ of a region delimited by two Rushton impellers. All of the vectors are shown with the same length, and the color-coding is based on the velocity magnitude (blue and red vectors correspond to low and high velocities, respectively). The calculated velocity field is able to capture key features of the flow, such as the size of the yielded regions (caverns), the location of strong tangential lines, and the loca-

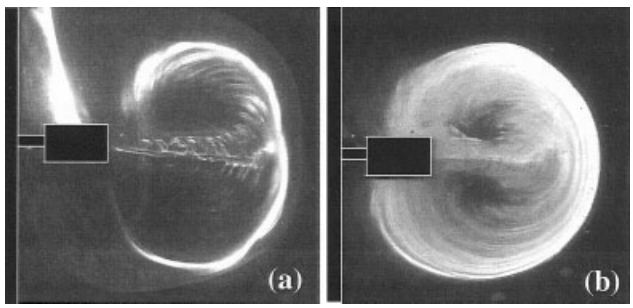


**Figure 8. (a) Tracer visualization using pLIF of a shear-thinning yield stress fluid in a tank stirred by a Rushton impeller at $Re' = 35.1$.**

The snapshot reveals stretching, folding, and lobe formation after 60 s. (b) Visualization of the same flow after 1 min of agitation shows the invariance of the mixing structure.

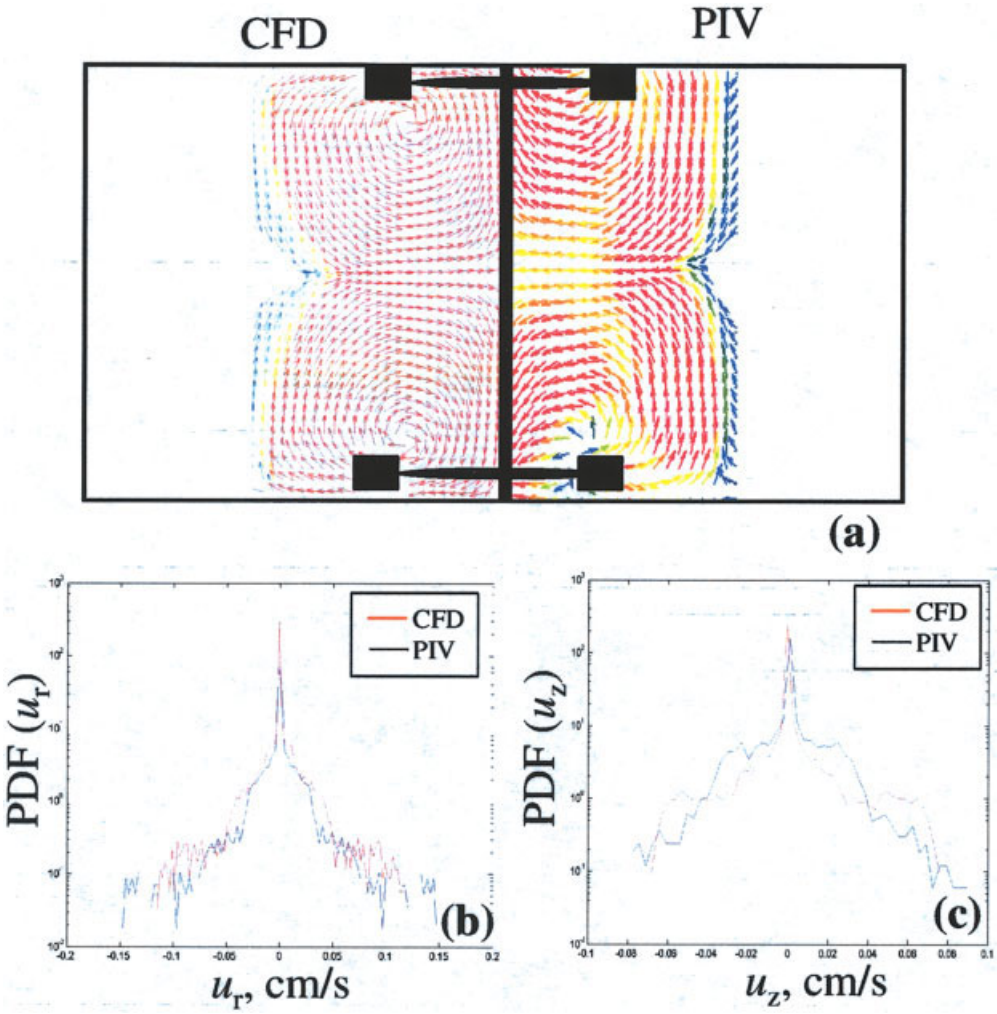


**Figure 9. (a) Instantaneous velocity fields obtained via numerical simulation (lefthand side) and experiments (righthand side) in a region between the upper and middle impeller at $Re' = 35.1$.**

Simulations seem to capture the main flow patterns, such as the size of the unyielded regions and the direction of the flow. Both experimental and simulated instantaneous velocity fields are compared by examining the probability density function (PDF) of their (b) radial and (c) axial velocities. [Color figure can be viewed in the online issue, which is available at www.interscience.wiley.com.]

tion of re-circulation regions. Another way to assess the agreement between numerical simulations and PIV is by computing the probability density function (PDF) of their velocity components. The PDF of the radial ($u_r$) and axial ($u_z$) components of the velocity are shown in Figures 9b and 9c, respectively. The discrepancy between CFD and PIV can be quantified in terms of the root-mean-square (RMS) deviation:

$$\mathrm{RMS} = \frac{\left[\frac{1}{i}\Sigma_1^i\,(u_{Num} - u_{PIV})^2\right]^{1/2}}{\left[\frac{1}{i}\Sigma_1^i\,(u_{PIV})^2\right]^{1/2}}, \qquad (3)$$

where $i$ is the number of nodes in the velocity field. The RMS value is 6.2% and 8.3% for $u_z$ and $u_r$, respectively. The majority of the discrepancies are concentrated near boundaries (next to the impeller and walls), in regions of very slow velocities (near stagnant regions), and in the presence of the solid/liquid interfaces.

We find that the numerical simulations are able to capture the experimentally observed caverns and their behavior as a function of $Re'$. Figure 10 shows a comparison between UV visualization experiment (lefthand side of each figure) and particle tracking visualization using CFD (righthand side) at $Re' = 1.7$, $Re' = 11.7$, and $Re' = 35.1$, corresponding to Figures 10a, 10b, and 10c, respectively. Cavern formation is captured numerically by releasing tracer particles next to the impeller tip and allowing them to evolve for a certain period of time. Simulated particles are color-coded to match experimental data. We find that numerical simulations are able to accurately predict cavern size, shape, and location as a function of $Re'$. Numerical simulations are also able to capture the segregation between caverns; green particles in the middle cavern do not leave, and red particles in the upper and lower caverns do not penetrate the middle one.

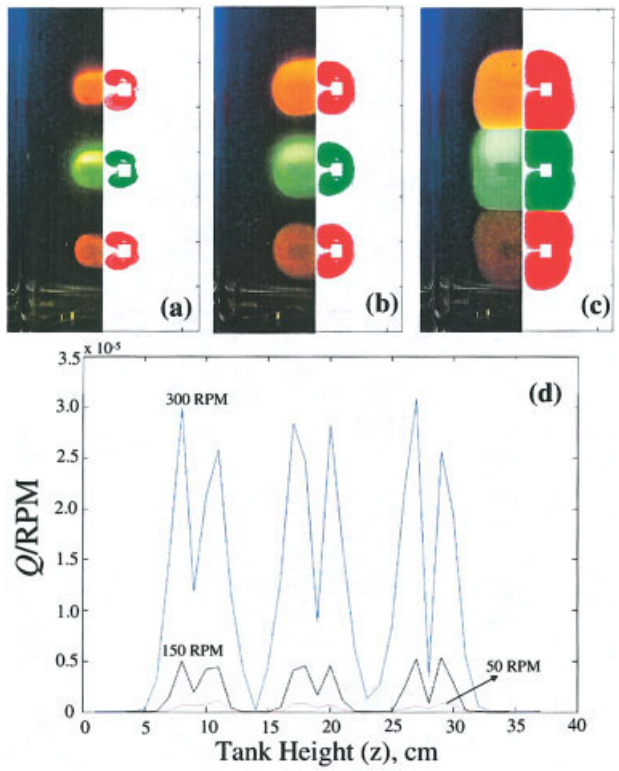


**Figure 10. Bulk flow behavior obtained via UV fluorescence (lefthand side) and numerical simulations (righthand side) at (a) $Re'$ = 1.7 (50 RPM), (b) $Re'$ = 11.7 (150 RPM), and (c) $Re'$ = 35.1 (300 RPM).**

Simulations are able to capture cavern formation and the strong cavern-cavern segregation. (d) Circulation velocity, $Q$, normalized by RPM shows strong separatrixes half-way between impellers, which is probably related to cavern-cavern segregation. [Color figure can be viewed in the online issue, which is available at www.interscience.wiley.com.]

As shown both by experiments and numerical simulations, the flow of a shear-thinning yield stress fluid in a multi-impeller system possesses separatrices that forbid passage of material from one cavern to another; the flow is strongly compartmentalized. This suggests that there is very little axial (vertical) flow near the tangential lines. We quantify axial flow by calculating the circulation velocity, $Q$, defined as $Q = 1/2 < |u_z\ (r)| >$. The quantity $Q$ is computed along cross sections of the vessel in the radial direction. Here, we compute $Q$ at 35 cross sections for $Re'$ = 1.7 (50 RPM), $Re'$ = 11.7 (150 RPM), and $Re'$ = 35.1 (300 RPM). The planes are equally spaced in the vertical direction spanning the entire vessel. Figure 10d illustrates the curves of $Q$/RPM as a function of vertical height. Recall that z = 0 cm and z = 36 cm correspond to the bottom and top of the vessel, respectively. The impellers are located at z = 9 cm, z = 18 cm, and z = 27 cm. The quantity $Q$/RPM must be equal to zero at z = 0 cm and z = 36 cm because the vessel is a batch system and no fluid can transverse the horizontal cross section at these locations.

For all the $Re'$ investigated here, the absolute minimum of $Q$/RPM for the internal planes exists at z = 13.5 cm and z = 22.5 cm, although they are not exactly zero. These are the mid-distances between impellers, revealing that there is minimum axial flow in those regions, which correspond to the separatrices between caverns. There are three additional local minima within the caverns corresponding to the impeller mid-plane at z = 8.5 cm, z = 17.5 cm, and z = 26.5 cm, which correspond to the lower, center, and upper impeller, respectively. In a perfectly symmetric and purely convective flow, these local minima would be zero and the lower and upper regions of the cavern would not communicate at all. The asymmetry of the boundary condition is what allows the finite axial communication within the caverns, although it is not strong enough to allow for any practical mixing between caverns. This suggests that introducing asymmetry into the system geometry would enhance vertical mixing in this flow. We will explore this possibility later in this article.

The mixing mechanism of shear-thinning viscoplastic fluids is investigated numerically by computing Poincaré sections of the flow inside the cavern. Poincaré sections are computed by aligning a lattice of particles along the impeller shaft and releasing them to the flow. We then considerer stroboscopic snapshots of particle trajectories and plot all particle intersections with a vertical plane on a single graph. Note that this method is analogous to pLIF experiments. Particle trajectories are computed for 300 impeller revolutions for $Re'$ = 35.1. At the end of this process, we observed toroidal regions above and below the impellers surrounded by a sea of chaos (Figure 11a); chaotic regions appear as seemingly random clouds of points, and regular (segregated) regions manifest themselves as regions devoid of points or close loops. The asymptotic mixing structure and the size and location of the toroidal regions in the computed Poincaré section agree with the experimental pLIF results (Figure 8b).

The mixing mechanism inside caverns can be further investigated by plotting particle trajectories as a function of impeller revolutions as shown for 5, 10, and 75 revolutions at $Re'$ = 35.1, corresponding to Figures 11b, 11c, and 11d, respectively. At 5 revolutions, we observe the formation of lobes that are ejected outward from the impeller in self-similar fashion. Later, the structure is filled with more material, but the main flow structure is conserved. This is similar to experimental images presented in Figures 4 and 8. This result indicates the presence of chaotic motion of fluid particles and suggests that physical mechanisms responsible for mixing of shear-thinning yield stress fluids is governed by stretching, folding, and lobe transport.

### *Stretching*

One of the key properties of flows exhibiting chaotic advection is the exponential divergence of nearby trajectories in real space, usually characterized by the largest local finite time Lyapunov exponent $\lambda$ over a time interval $\Delta t$. The Lyapunov exponent $\lambda$ is closely related to the stretching of fluid elements, which is a measure of mixing "performance"; high values of stretching usually mean "good" mixing. In this work, stretching computations are performed by placing small vectors in the flow. Usually, $5 \times 10^4$ vectors are used. Each vector located initially at $(r, z, \theta)$ is deformed by the instantaneous velocity gradient along its trajectory while being convected throughout the flow domain. Stretching $S$ is defined by the ratio of the vector final magnitude to its initial magnitude after $\Delta t$. Then $\lambda = (\log S)/\Delta t$. For time-periodic flows, the stretching field is

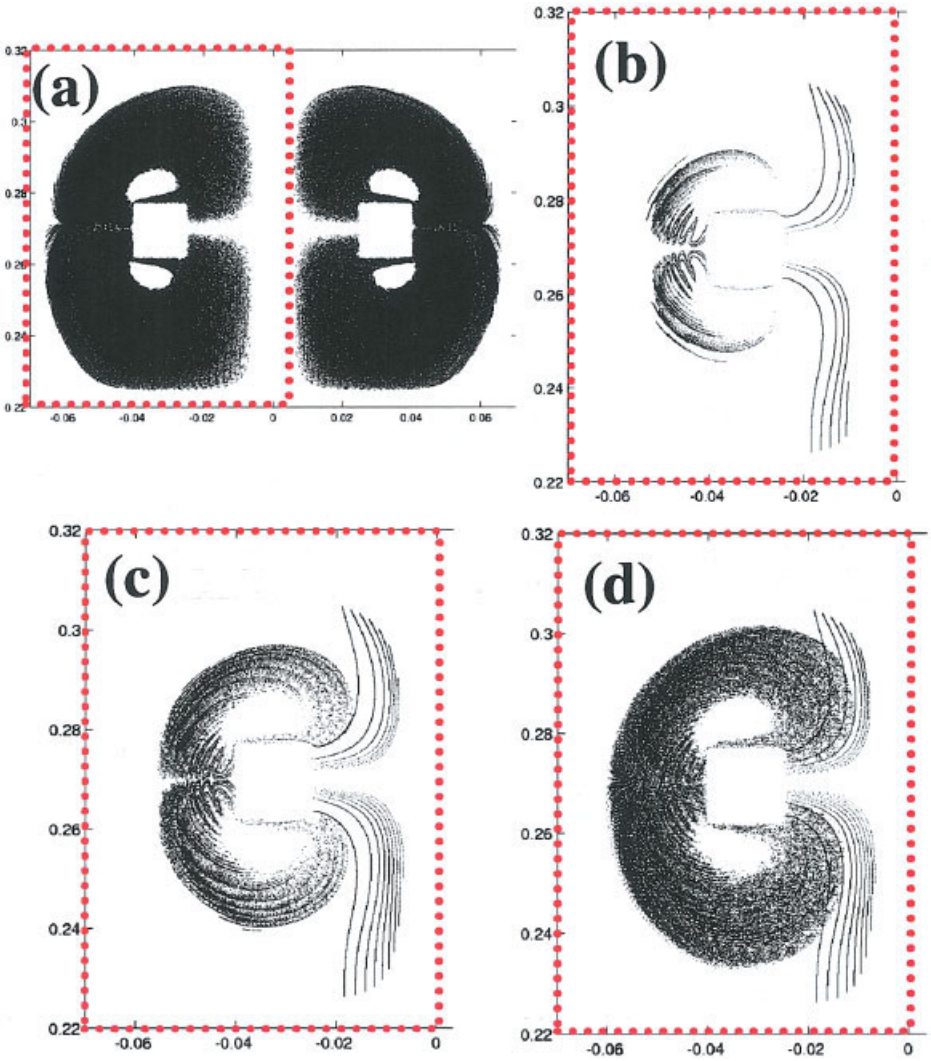


**Figure 11. Poincaré section of a shear-thinning yield stress fluid obtained by numerical simulations at $Re' = 35.1$.**

(a) Asymptotic structure reveals chaos and segregated regions inside caverns. Flow micro-structure in a region of interest shown in (a) at (b) 5 revs, (c) 10 revs, and (d) 75 revs. [Color figure can be viewed in the online issue, which is available at www.interscience.wiley.com.]

also a function of phase, but it is typically sufficient to focus attention on a single phase. Additional details on stretching computations can be found elsewhere.[4,36,42]

Figures 12a and 12b show stretching fields for $Re' = 11.7$ and $Re' = 35.1$, respectively, for the vertical plane aligned with one of the impeller blades. The fields are computed after 20 revolutions ($N = 20$). Only the bottom right half of the tank is presented in the figure. We do not assume any top-bottom or left-right symmetry in the calculations. Values of $S$ are color coded; the points with the lowest value of $S$ are in dark blue, while red corresponds to the highest value of $S$. The highest values of $S$ are concentrated within the caverns in the yielded region; the unyielded region contains most of the lowest values of $S$. The region containing high values of $S$ grows with $Re'$. We find a resemblance between the stretching field patterns and the computed (Figure 11) and experimental (Figure 8) mixing patterns such as the presence of lobes and segregated regions. There is, however, significant heterogeneity of $S$ values within the yielded region (caverns).

The statistical distributions of the stretching are shown in Figure 13a for an $Re' = 35.1$ case at different $N$. Because the logarithm of the stretching is proportional to the distribution of finite time Lyapunov exponents, we actually plot the probability density function (PDF) of log $S$, rather than the PDF of $S$ itself. The PDF of log $S$ is defined as $H(\log S) = \mathrm{d}n(\log S)/\mathrm{d}(\log S)$, where $\mathrm{d}n(\log S)$ is the number of points with values of log $S$ between log $S$ and log $S$ + d(log $S$). It may be seen that for all of the flows, the distributions are double peaked. The low stretching value peaks correspond to the size of the stagnation zone plus any regular region found inside the cavern. We find that the area under the curve corresponding to low stretching values decreases only slightly as $N$ is increased. This is due to the slow stretching of small numbers of vectors inside the yielded region. The high stretching peaks correspond to the caverns. The distributions are quite broad and span several decades, which indicate strong spatial heterogeneity of $S$ within the yielded region (caverns). The distributions tend to get broader as the number of revolutions over which they are computed increases. They also shift toward higher values with increasing $N$.

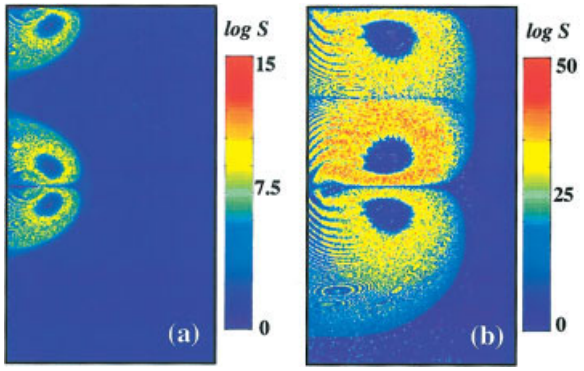


**Figure 12. Stretching fields corresponding to the lower, right-half part of the tank at (a) $Re'$ = 11.7 and (b) $Re'$ = 35.1 computed after 20 revolutions ($N$ = 20).**

The flow produces stretching fields with similar features as the mixing patterns. Note the presence of segregated regions and lobes. There is also significant heterogeneity in stretching values inside the caverns. [Color figure can be viewed in the online issue, which is available at www.interscience.wiley.com.]

The data in Figure 13a suggest that $S$ fields may have similar structure at different $N$; the spatial distribution of $S$ values may be self-similar with respect to mixing time (or $N$). We explore the scaling properties of these distributions by rescaling the logarithm of the stretching values by the logarithm of the geometrical mean of the stretching ($S_g$). The logarithm of the geometric mean stretching is equivalent to the arithmetic mean of log $S$:

$$\log S_g = \frac{\int (\log S) H(\log S) d \log S}{\int H(\log S) d \log S}. \quad (4)$$

The results for the distribution of the rescaled stretching values are displayed in Figure 13b, where we introduce a variable $p = (\log S)/(\log S_g)$. This quantity $p$ is equivalent to $(\log S)/(<\lambda>\Delta t)$, where $<\lambda>$ is the average finite time Lyapunov exponent. It may be seen that there is a substantial degree of collapse of the distributions for each of the flows, although it is not perfect. In Figure 13b, the rescaled stretching distributions are nearly identical for large $N$, as one might expect. Note that the frequency of occurrence of $S = 1$ or $\log S = 0$ (that is, no stretching) is non-zero; this indicates that some regions of these flows are not chaotic. This high degree of collapse indicates that the mixing process is self-similar in time and that the above mentioned heterogeneity of $S$ are permanent features of this flow. Similar statistical properties of stretching fields have been recently observed in experiments for time-periodic chaotic flows in 2D.[43]

### *Scaling with respect to size*

A distinct challenge faced by engineers is the prediction of mixing performance upon scaling with respect to vessel size. This section demonstrates the use of numerical simulations for scale-up analysis and prediction by measuring the cavern size created by a single Rushton impeller in four tanks of different sizes. The volumetric tank sizes are 15 L, 75 L, 300 L, and 750 L. Each tank is geometrically similar with a height to diameter ratio of 1.38:1 and has a standard Rushton turbine located at the middle of the tank. We compute the cavern size directly from the velocity field by defining a threshold velocity ($u_{thresh}$) of $5 \times 10^{-4}$ m/s. Any region of the velocity field with velocities less than $u_{thresh}$ is considered stagnant. Cavern size is quantified as the volume fraction ($V_c$) of fluid with velocities higher than or equal to $u_{thresh}$.

The non-Newtonian Reynolds number, $Re'$, facilitates comparison of cavern size at different scales. Figure 14a shows the normalized volume fraction $V_c/V_T$, where $V_T$ is the tank volume, as a function of $Re'$ for each of the tank sizes. The data span a range of impeller speeds (that is, shear rates) that correspond to the cavern not extending to the tank wall at low impeller speeds and extensive contact between the wall and cavern at higher speeds. At each scale, the cavern size follows a consistent trend with $Re'$ based upon the apparent viscosity at

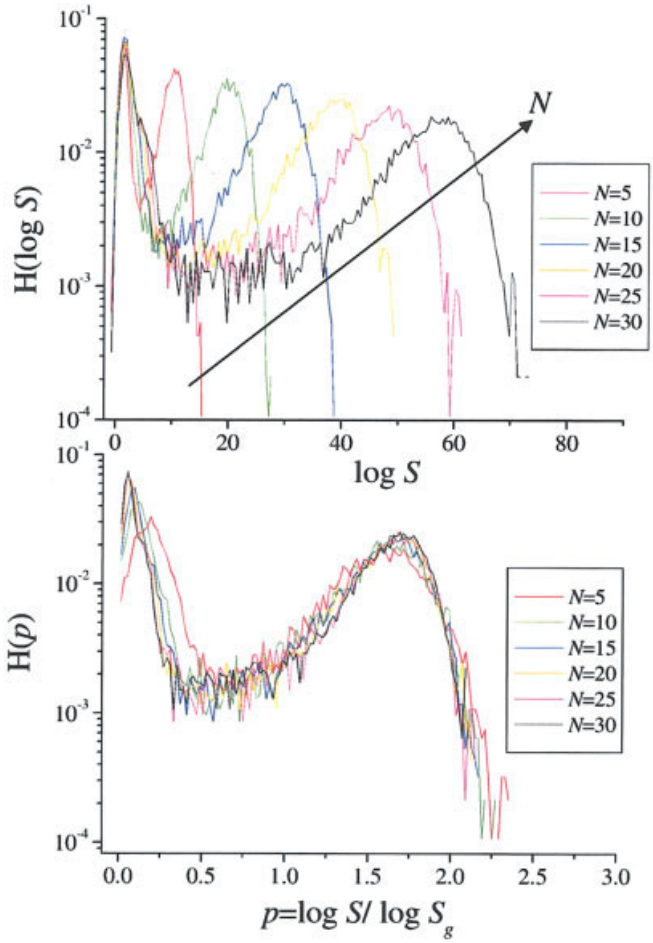


**Figure 13. (a) Probability density function of the logarithm of stretching $S$, computed over the entire flow at various $N$ at $Re'$ = 35.1: $N$ = 5(red), 10 (green), 15 (blue), 20 (orange), 25 (purple), and 30 (black).**

Values of $S$ show strong heterogeneity spanning many decades. All of the distributions have similar double-peaked shapes and become wider for large $N$. (b) Curves collapse after normalization, revealing the invariance of the distribution. [Color figure can be viewed in the online issue, which is available at www.interscience.wiley.com.]

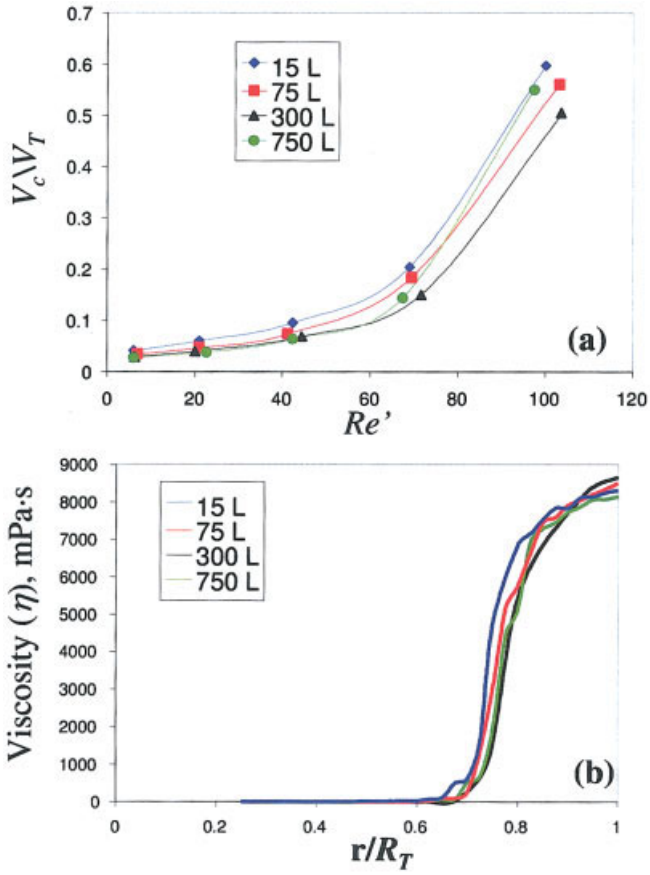


**Figure 14. Scaling with vessel size.**

(a) Normalized cavern volume ($V_c/V_T$) as a function of $Re'$ for different vessel sizes. (b) Radial viscosity profile, $\eta$(r), for different size tanks at constant $Re'$. Cavern boundary exists at equivalent locations on the normalized scale. [Color figure can be viewed in the online issue, which is available at www.interscience.wiley.com.]

the tip of the impeller blade. The analysis with this dimensionless parameter effectively collapses the performance to a single curve. The numerical curve trend is very similar to the experimental data shown in Figure 5c. Note that in Figure 5c we measure area, while simulations measure volume.

Self-similar behavior on scale-up is further evident when the radial viscosity profile, $\eta$(r), is examined in different size tanks at constant $Re'$. Figure 14b shows the average viscosity as a function of radius in the middle of geometrically similar 15 L, 75 L, 300 L, and 750 L tanks operated at $Re' = 42$. The plot normalizes the radial location (r) with the tank radius ($R_T$). The curves match closely and show that the cavern boundary exists at equivalent locations on the normalized scale.

The data shown in Figure 14 apply only for vessels with equivalent geometrical parameters. In practice, however, the geometries of lab-scale experiments do not always match the large-scale equipment configuration due to constraints of materials of construction or prohibitive costs of building custom devices. Numerical simulations, such as the one presented in this work, may provide tools to overcome this challenge.

## Enhancing Mixing of Shear-Thinning Yield Stress Fluids

Experiments and numerical simulations show the presence of persistent separatrices between caverns in multi-impeller systems (Figure 10), even at high $Re'$. These separatrices constitute the main impediment to efficient mixing of shear-thinning yield stress fluids in multi-impeller system. Hence, it is necessary to design mixing protocols that are able to break such separatrices.

In general, flow separatrices can be a result of symmetries that constrain the velocity field. Different approaches to overcome inefficient mixing based on breaking either temporal or spatial symmetry have been proposed.[44-46] Recently, it has been demonstrated that for some values of geometrical eccentricity in stirred tanks, widespread chaos is achieved and a significant reduction in mixing time is observed with respect to concentric systems[47]; the authors also observed a significant enhancement of axial velocity.

We examine the effect of breaking spatial symmetry of shear-thinning viscoplastic fluids in stirred tanks by placing the impeller shaft 5.082 cm from the centerline. Eccentricity is defined as $E = \beta/R_T$ where $R_T$ is the tank radius and $\beta$ is the distance from the shaft to the centerline. Velocity measurements are performed on both concentric ($E = 0$) and eccentric systems ($E = 0.42$) at $Re' = 61.4$, as shown in Figures 15a and 15b, respectively. Under eccentric conditions, we find that the symmetry of the velocity field is broken (Figure 15b) and the axial component of the velocity is apparently enhanced.

We quantify this enhancement by comparing the PDF of the normalized axial velocities for both the eccentric and concentric systems (Figure 15c). Axial velocity is normalized by its respective standard deviation ($u_z/\sigma$). The data show that, in the eccentric case, the frequency of most non-zero axial velocity values increases and the curve spreads over a larger range of non-negative velocities.

Mixing performance in an eccentric system is assessed using tracer experiments. A small blob of passive dye is injected 2 cm above and to the right of the center impeller mid-plane. The evolution of the passive dye is shown at 60 s, 120 s, and 320 s in Figures 16a through 16c, respectively. Figure 16a shows that the cavern structure becomes asymmetric and extends axially. The flow microstructure inside the caverns possesses the same characteristics of the concentric case, with the presence of lobe structures and small toroidal regions. However, dye seems to "escape" to the upper and lower caverns. In Figure 16b, we clearly observe that dye reaches the upper cavern, which indicates that the flow separatrix between caverns is perturbed. Although signs of inefficient mixing are still present at later times (Figure 16c), such as the uneven distribution of dye concentration, we find that breaking spatial symmetry seems to significantly improve cavern-cavern segregation.

## Summary and Conclusions

In this article, we present an experimental and numerical investigation of mixing of shear-thinning fluids with yield stress in stirred tanks. Mixing is characterized in experiments by means of velocity measurements and tracer visualization. Experiments reveal familiar bulk-flow behavior characterized by the formation of caverns around impellers (Figure 5). In multi-impeller systems, we find strong separatrices that lead to

robust segregation between caverns (Figure 6). These separatrices are the main obstacles for global mixing in shear-thinning yield stress fluids in stirred tanks. Velocity field measurements show strong tangential lines and re-circulation loops above and below the impeller (Figure 7). Flow microstructures show the emergence of self-similar mixing patterns, stretching, folding, and lobe transport, all classically associated with chaotic mixing (Figure 8).

Numerical simulations of shear-thinning yield stress fluids seem to capture the essential features of the flow, such as cavern formation and cavern-cavern segregation (Figure 10). Computed Poincaré sections show the experimentally observed flow microstructure, such as the presence of lobe formation (Figure 11). The potential for efficient mixing is examined by computing stretching fields (Figure 12), which reveals self-similar behavior as a function of $Re'$ (Figure 13). Scaling behavior with respect to size is investigated using numerical simulations. These show that strong boundaries between adjacent caverns are expected even at high agitation speeds (Figure 14).

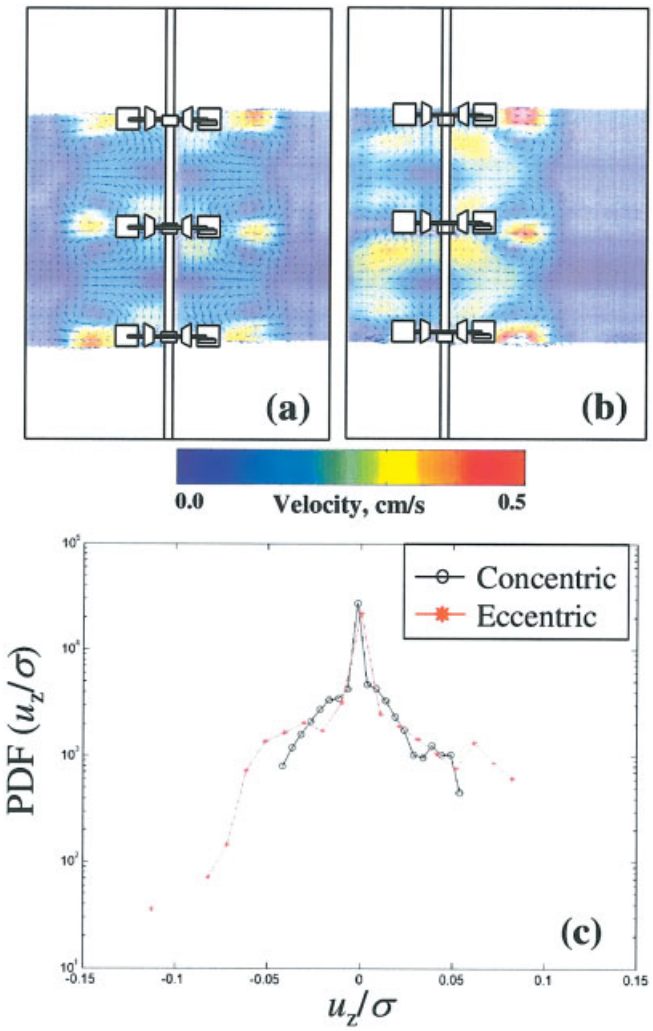


**Figure 15. Experimental instantaneous velocity fields obtained for (a) concentric and (b) eccentric case ($E = 0.42$) at $Re' = 61.4$.**

(c) Comparison of the normalized axial velocities PDF between concentric and eccentric systems. Significant enhancement of the axial velocities is observed for the eccentric case. [Color figure can be viewed in the online issue, which is available at www.interscience.wiley.com.]

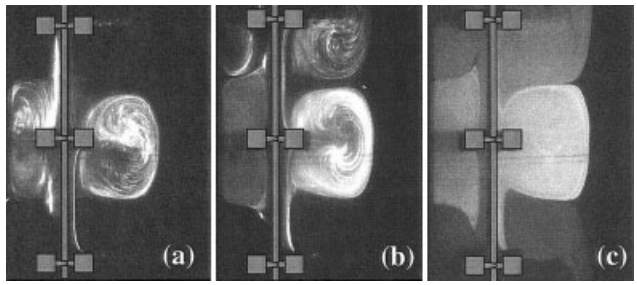


**Figure 16. Evolution of mixing structures in an eccentric tank ($E = 0.42$) at $Re' = 61.4$.**

Snapshots are taken at (a) 60 s, (b) 120 s, and (c) 320 s. Mixing between caverns is observed.

Finally, a mixing protocol based on symmetry-breaking is investigated for its effectiveness to destroy cavern-cavern segregation. By positioning the impellers in an eccentric configuration, we find: (i) enhancement of axial velocities (Figure 15) and (ii) appreciable mixing between distinct caverns (Figure 16).

The experimental and numerical results presented here show that in the range of Reynolds numbers investigated the mixing of shear-thinning yield stress fluids is controlled by chaotic dynamics. Very strong tangential lines leading to cavern-cavern segregation are found in multi-impeller systems, which to the best of our knowledge were not previously reported. This result is of importance since many fluids of industrial interest, such as pastes, paints, suspensions, and cell broths, are shear-thinning and viscoplastic. However, it is not clear whether the strong tangential lines observed in the velocity fields are due to shear-thinning viscosity or yield stress behavior, or if cavern-cavern segregation is only present when both rheological behaviors are present. This remains to be investigated. Nevertheless, breaking spatial symmetry by positioning the impeller off-center weakens the segregation barrier and allows mixing between caverns.

## Acknowledgments

We appreciate many insightful discussions with T. Shinbrot. F. Shakib and K. Johnson provided helpful comments on numerical simulations. J. Kukura is funded by the Doctoral Study Program of Merck Research Laboratories.

## Literature Cited

1. Aref H. Stirring by chaotic advection. *J Fluid Mech.* 1984;143:1-21.
2. Gollub JP, Solomon TH. Complex particle trajectories and transport in stationary and periodic convective flows. *Physica Scripta.* 1989;40:430-435.
3. Mathieu J, Chevray R. *Topics in Fluid Mechanics*. Cambridge, UK: Cambridge University Press; 1993.
4. Muzzio FJ, Swanson PD. The statistics of stretching and stirring in chaotic flows. *Phys Fluids.* 1991;3:822-834.
5. Ottino JM. *The Kinematics of Mixing: Stretching, Chaos, and Transport*. Cambridge, UK: Cambridge University Press; 1989.
6. Solomon TH, Weeks ER, Swinney HL. Chaotic advection in a two-dimensional flow: Levy flights and anomalous diffusion. *Physica D.* 1994;76:70-84.

7. Swanson PD, Ottino JM. A comparative computational and experimental study of chaotic mixing of viscous fluids. *J Fluid Mech.* 1990;213:227-249.
8. Barnes HA. The yield stress—a review or '$\pi\alpha\nu\tau\alpha\ \rho\epsilon\iota$'—everything flows? *J Non-Newtonian Fluid Mech.* 1999;81:137-178.
9. Wichterle K, Wein O. Threshold of mixing of non-Newtonian fluids. *Inter Chem Eng J.* 1981;21:116-120.
10. Curran SJ, Hayes RE, Afacan A, Williams MC, Tanguy PA. Experimental mixing study of a yield stress fluid in a laminar stirred tank. *Ind Eng Chem Res.* 2000;39:195-202.
11. Doucet L, Ascanio G, Tanguy PA. Hydrodynamic characterization of rotor-stator mixer with viscous fluids. *Chem Eng Res Des.* 2005;83: 1186-1195.
12. Elson TP. The growth of caverns formed around rotating impellers during the mixing of a yield stress fluid. *Chem Eng Commun.* 1990; 41:2555-2562.
13. Tanguy PA, Bertrand F, Labrie R, Brito-De La Fuente E. Numerical modeling of the mixing of viscoplastic slurries in a twin blade planetary mixer. *Chem Eng Res Des.* 1996;74:499-504.
14. Torres LG, Flores F, Galindo E. Apparent yield stress of xanthan solutions and broths. *Bioproc Eng.* 1995;12:41-46.
15. Amanullah A, Serrano-Carreon L, Castro B, Galindo E, Nienow AW. The influence of impeller type in pilot scale xanthan fermentations. *Biotech & Bioeng.* 1998;57:95-108.
16. Moore IPT, Cossor G, Baker MR. Velocity distribution in a stirred tank containing a yield stress fluid. *Chem Eng Sci.* 1995;50:2467-2481.
17. Dieulot JY, Petit N, Rouchon P, Delaplace G. An arrangement of ideal zones with shifting boundaries as a way to model mixing processes in unsteady stirring conditions in agitated vessels. *Chem Eng Sci.* 2005; 60:5544-5554.
18. Harvey AD, Rogers SE. Steady and unsteady computation of impeller-stirred reactors. *AIChE J.* 1996;42:2701-2712.
19. Raman V, Fox RO, Harvey AD, West DH. CFD analysis of premixed methane chlorination reactors with detailed chemistry. *Ind Eng Chem Res.* 2001;40:5170-5176.
20. Raut JS, Naik VM, Jongen TR. Efficient simulation of time-dependent flows: application to a twin screw extruder. *AIChE J.* 2003;49:1933-1946.
21. Zalc JM, Alvarez MM, Muzzio FJ, Arik BE. Extensive validation of computed laminar flow in a stirred tank with three Rushton turbines. *AIChE J.* 2001;47:2144-2154.
22. Bittleston SH, Hassger O. Flow of viscoplastic fluids in a rotating concentric annulus. *J Non-Newtonian Fluid Mech.* 1992;42:19-36.
23. Escudier MP, Oliveira PJ, Pinho FT. Fully developed laminar flow of purely viscous non-Newtonian liquids through annuli, including the effects of eccentricity and inner-cylinder rotation. *Int J Heat & Fluid Flow.* 2002;23:52-73.
24. Fan Y, Phan-Thien N, Tanner RI. Tangential flow and advective mixing of viscoplastic fluids between eccentric cylinders. *J Fluid Mech.* 2001;431:65-89.
25. Fang P, Manglik RM, Jog MA. Characteristics of laminar viscous shear-thinning fluid flows in eccentric annular channels. *J Non-Newtonian Fluid Mech.* 1999;84:1-17.
26. Fradette L, Huai ZL, Choplin L. 3-D finite element simulation of fluid flow through a SMX static mixer. *Comput Chem Eng.* 1998;22:5759-5761.
27. Pericleous KA, Patel MK. Industrial and environmental modeling of non-Newtonian fluid flows. *Ind Env Appl Fluid Mech.* 1999;145:133-144.
28. Aubin J, Naude I, Bertrand J, Xuereb C. Blending of Newtonian and shear-thinning fluids in a tank stirred with a helical screw agitator. *Chem Eng Res Des.* 2000;78:1105-1114.
29. Deshpande NS, Barigou M. Vibrational flow of non-Newtonian fluids. *Chem Eng Sci.* 2001;56:3845-3853.
30. Arratia PE, Muzzio FJ. Planar laser-induced fluorescence method for analysis of mixing in laminar flows. *Ind Eng Chem Res.* 2004;43:6557-6568.
31. Papanastasiou TC. Flow of materials with yield. *J Rheol.* 1987;31: 385-404.
32. Alexandrou AN, Duc E, Entov V. Inertial, viscous, and yield-stress effects in Bingham fluid filling of a 2-D cavity. *J Non-Newtonian Fluid Mech.* 2001;96:383-403.
33. Burgos GR, Alexandrou AN. Flow development of Herschel-Bulkley fluids in a sudden 3-D square expansion. *J Rheol.* 1999;43:485-498.
34. Alvarez MM, Zalc JM, Arratia PE, Shinbrot T, Muzzio FJ. The mechanism of mixing and creation of structure in laminar stirred tanks. *AIChE J.* 2002;48:2135-2148.
35. Yao WG, Sato H, Takahashi K, Koyama K. Mixing performance experiments in impeller stirred tanks subjected to unsteady rotational speeds. *Chem Eng Sci.* 1998;53:3031-3040.
36. Zalc JM, Szalai ES, Alvarez MM, Muzzio FJ. Using CFD to understand chaotic mixing in laminar stirred tanks. *AIChE J.* 2002;48:2124-2134.
37. Bresler L, Shinbrot T, Metcalfe G, Ottino JM. Isolated mixing regions: origin, robustness and control. *Chem Eng Sci.* 1997;52:1623--1636.
38. Nienow AW, Elson TP. Aspects of mixing in rheologically complex fluids. *Chem Eng Res Des.* 1988;66:5-15.
39. Images are assigned a pixel value threshold equivalent to regions of the tank with no dye. Any pixel with values higher than the threshold value is considered active and counted to measure cavern size.
40. Arratia PE, Alvarez MM, Shinbrot T, Muzzio FJ. Mixing of non-Newtonian fluids in steadily forced systems. *Phys Rev Lett.* 2005;94: 084501-1–084501-4.
41. Lamberto DJ, Alvarez MM, Muzzio FJ. Experimental and computational investigation of the laminar flow structure in a stirred tank. *Chem Eng Sci.* 1999;54:919-942.
42. Szalai ES, Muzzio FJ. Predicting mixing microstructure in three-dimensional chaotic systems. *Phys Fluids.* 2003;15:3274-3279.
43. Arratia PE, Gollub JP. Statistics of stretching fields in experimental fluid flows exhibiting chaotic advection. *J Stat Phys.* 2005;121:805-822.
44. Fountain GO, Khakhar DV, Ottino J, M. Visualization of three-dimensional chaos. *Science.* 1998;281:683-686.
45. Lamberto DJ. Enhancing laminar mixing in stirred tank reactors using dynamical flow perturbations, PhD Thesis, Rutgers University, 1997.
46. Voth GA, Saint TC, Dobler G, Gollub JP. Mixing rates and symmetry breaking in two-dimensional chaotic flow. *Phys Fluids.* 2003;15:2560-2566.
47. Alvarez MM, Arratia PE, Muzzio FJ. Laminar mixing in eccentric stirred tank systems. *Can J Chem Eng.* 2002;80:546-557.

*Manuscript received Aug. 9, 2005, and revision received Feb. 26, 2006.*